AGU PUBLICATIONS

JGR

Journal of Geophysical Research: Atmospheres

RESEARCH ARTICLE
10.1002/2013JD020689

Key Points:
- We proposed a new algorithm for retrieving global bare soil BBE
- We presented the strategy for generating global land surface BBE
- Generate global 8 day 1 km global land surface BBE using the strategy

Correspondence to:
J. Cheng,
brucechan2003@126.com

Citation:
Cheng, J., and S. Liang (2014), Estimating the broadband longwave emissivity of global bare soil from the MODIS shortwave albedo product, *J. Geophys. Res. Atmos.*, *119*, 614–634, doi:10.1002/2013JD020689.

Received 4 AUG 2013
Accepted 1 OCT 2013
Accepted article online 30 JAN 2014
Published online 30 JAN 2014

Estimating the broadband longwave emissivity of global bare soil from the MODIS shortwave albedo product

Jie Cheng[1] and Shunlin Liang[1,2]

[1]State Key Laboratory of Remote Sensing Science, College of Global Change and Earth System Science, Beijing Normal University, Beijing, China, [2]Department of Geographical Science, University of Maryland, College Park, Maryland, USA

Abstract A constant land surface longwave emissivity value, or very simple parameterization, has been adopted by current land surface models because of a current lack of reliable observations. Of all the various Earth surface types, bare soil has the highest variations in broadband emissivity (BBE). We propose here a new algorithm to estimate BBE in the 8–13.5 μm spectral range based on the Moderate Resolution Imaging Spectrometer (MODIS) albedo product for bare soil. This algorithm takes advantage of both Advanced Spaceborne Thermal Emission and Reflection Radiometer (ASTER) longwave emissivity and MODIS shortwave albedo products, as well as the established linear relationship between ASTER BBE and seven MODIS spectral albedos for bare soil. In order to mitigate step discontinuities in the global land surface BBE product, a transition zone was established and the BBE estimation method was also provided. Three linear formulae were derived for bare soil and transition zones, respectively. Given the accuracy of 0.01 for MODIS spectral albedo, the absolute accuracy of BBE retrieval is better than 0.017. The validation results obtained from the three field trials conducted in China and one field trial in western/southwestern U.S. indicated that the average difference between the estimated BBE and the measured BBE was 0.016. We have introduced a new strategy to generate global land surface BBE using MODIS data. This strategy was used to generate global 8 day 1 km land surface BBE products from 2000 through 2010.

1. Introduction

Surface broadband emissivity (BBE) is a key variable for estimating surface longwave net radiation, which is a component of the surface radiation budget and an important parameter in climate, weather, and hydrological models [*Cheng et al.*, 2010b; *Jacob et al.*, 2004; *Jin and Liang*, 2006; *Liang*, 2004; *Liang et al.*, 2010; *Pequignot et al.*, 2008; *Sellers et al.*, 1997]. However, due to the lack of reliable observations, a constant emissivity value or very simple parameterizations are currently used in land surface models and general circulation models [*Bonan et al.*, 2002; *Jin and Liang*, 2006; *Zhou et al.*, 2003b]. For example, the National Center for Atmospheric Research Community Land Model Version 2 calculates the canopy emissivity from the leaf area index and sets the soil and snow emissivities as 0.96 and 0.97, respectively [*Bonan et al.*, 2002]. A study of the simulated energy balance sensitivity to changes in emissivity over North Africa and the Arabian Peninsula showed that a decrease of 0.1 in the soil BBE increased the ground and air temperatures by an average of approximately 1.1 and 0.8°C, respectively, while decreases in the net and upward longwave radiation were about 6.6 and 8.1 W/m^{-2}, respectively [*Zhou et al.*, 2003b]. Jin and Liang also demonstrated the contributions of BBE in improving the simulation results of climate models [*Jin and Liang*, 2006].

BBE, with its finer spatial resolution and higher temporal resolution, will be useful for surface energy balance studies at local scales and serves as medium scale for the validation of coarse resolution data thereby improving our understanding of land-atmosphere interactions [*Liang*, 2011; *Ogawa and Schmugge*, 2004; *Ogawa et al.*, 2008]. Several studies have mapped the land surface BBE at global or regional scales. Wilber et al. generated a global BBE (5–100 μm) map with a 10 minute spatial resolution based on land cover type [*Wilber et al.*, 1999]. Ogawa et al. mapped the global monthly BBE (8–13.5 μm) using the Moderate Resolution Imaging Spectrometer (MODIS) emissivity product (approximately 5 km) and a North African BBE (8–13.5 μm) map using the Advanced Spaceborne Thermal Emission and Reflection Radiometer (ASTER) emissivity product (90 m) [*Ogawa and Schmugge*, 2004; *Ogawa et al.*, 2008]. Peres et al. produced a global BBE (3–14 μm) map at a 3 km spatial resolution by converting the narrowband emissivities retrieved from the Spinning

Enhanced Visible and Infrared Imager onboard Meteosat Second Generation with vegetation cover method [*Peres and DaCamara*, 2005]. However, the spatial resolutions or the temporal resolutions of these products are limited. To our knowledge, moderate spatial resolutions BBE on the order of 1 km are currently unavailable.

One method for generating a high spatiotemporal global BBE map is the conversion of satellite narrowband emissivity products. Unfortunately, surface temperature and emissivity retrieval from thermal infrared (TIR) radiometric measurements is an ill-posed problem, i.e., solving $N+1$ variables with N equations [*Kanani et al.*, 2007; *Li et al.*, 2013; *Liang*, 2001, 2004]. At least one additional equation must be created to regularize this ill-posed problem. The equation generated is usually based on empirical formulae or assumptions for which the solutions are likely to be unstable. This may be the reason why only a few land surface emissivity (LSE) retrieval algorithms proposed over the past 30 years have been selected as operational algorithms [*Borel*, 2008; *Cheng et al.*, 2010a; *Cheng et al.*, 2008; *Gillespie*, 1985; *Gillespie et al.*, 1998; *Griend and Owe*, 1993; *Li and Becker*, 1993; *Liang*, 2001; *Peres and DaCamara*, 2006; *Sobrino et al.*, 2008; *Valor and Caselles*, 1996; *Wan and Li*, 1997]. Another approach that deserves test application is the effort to establish quantitative relationships between the LSE and factors such as the chemical composition, water content, and microstructure of the land surface [*Hulley et al.*, 2010; *Mira et al.*, 2007; *Mushkin and Gillespie*, 2005; *Nerry et al.*, 1988; *Xiao et al.*, 2003]. However, such relationships do not hold true at a remote-sensing pixel scale.

The soil BBE (8–12 μm) varies substantially, ranging from 0.81 to 0.99 [*Ogawa et al.*, 2003]. An accurate estimation of soil emissivity is crucial when generating a global land surface emissivity record. Sobrino et al. established the linear relationship between narrowband emissivity and red reflectance for multiple thermal infrared sensors for bare soils [*Sobrino et al.*, 2008]. Tsvetsinskaya et al. found that the MODIS albedo is correlated with specific soil and geological features in North Africa and the Arabian Peninsula, which suggests that surface types can be used to characterize the albedo in those areas [*Tsvetsinskaya et al.*, 2002]. Zhou et al. showed that ASTER BBE (3–14 μm) has a correlation with each of MODIS seven narrowband and three broadband albedos for some specific surface types (10 soil suborders) in the North African desert [*Zhou et al.*, 2003a]. If this relationship holds true for other soil orders throughout the world, we can produce 8 day 1 km bare soil BBEs using the MODIS 8 day 1 km albedo, which would facilitate global BBE estimation.

The objective of this study was to explore the relationship between the Moderate Resolution Imaging Spectrometer (MODIS) albedo and the Advanced Spaceborne Thermal Emission and Reflection Radiometer (ASTER) BBE for bare soil at a global scale to facilitate the estimation of a global land surface BBE product. This idea has been used to estimate the BBE for vegetated area from MODIS albedo and to estimate the global BBE from the Advanced Very High Resolution Radiometer visible and near-infrared data [*Cheng and Liang*, 2013; *Ren et al.*, 2013].

The paper is arranged as follows. Section 2 exhibits the relationship between ASTER BBE and MODIS seven narrowband albedo and describes the method of estimating BBE for global bare soil; section 3 presents the retrieval results and error analysis; and section 4 shows the validation results. The schemes for producing global bare soil BBE are given in section 5, and a brief discussion and conclusion are provided in sections 6 and 7, respectively.

2. Methodology

2.1. Establishing the Relationship Between MODIS Shortwave Albedo and ASTER BBE

Zhou et al. investigated the relationship between MODIS albedo and ASTER BBE over a study area of 520 × 1400 km^2 in North Africa that covers Algeria, Libya, and Tunisia [*Zhou et al.*, 2003a]. The author derived seven spectral albedos and three broadband albedos from the MODIS albedo product from November 2011 to January 2012, and the ASTER BBE from the ASTER emissivity product ranging from 2000 to 2002 using a liner combination of ASTER five band emissivities [*Ogawa et al.*, 2003]. The MODIS albedo and ASTER BBE were reprojected to 2 min resolution to match the spatial resolution of the used soil taxonomy, which was used to extract the BBE-albedos pairs for each soil order. In total, 35,507 BBE-albedos pairs were obtained for nonvegetated pixels. A liner relationship was fitted for ASTER BBE and MODIS broadband albedo. The R^2 were 0.37, 0.61, and 0.58 for broadband albedo at 0.4–0.7 μm, 0.7–5.0 μm, and 0.4–5.0 μm spectral range, respectively. The R^2 for each spectral albedo and ASTER BBE varied from 0.03 (0.459–0.479 μm) to 0.72 (2.105–2.155 μm). The relationship for each soil order is similar to that derived using all soil orders.

Table 1. Spectral Bands and Their Wavelength Ranges of the MODIS Spectral Albedo

Spectral Bands	1	2	3	4	5	6	7
Wavelength ranges (μm)	0.62–0.67	0.84–0.87	0.46–0.48	0.54–0.56	1.23–1.25	1.63–1.65	2.11–2.15

We acquired the MODIS albedo product, vegetation index product, and ASTER emissivity product in North Africa (23.6°–37.5°N, 6°–14°E) that covers Algeria, Libya, and Tunisia from 2000 through 2002. During November 2001 and January 2002, a total of 223 ASTER scenes and 336 MODIS tiles were acquired. We derived 303,205 BBE-albedos pairs for bare soil (nonvegetated) using the normalization vegetation indices (NDVI) threshold of 0.156 according to a previous study [*Momeni and Saradjian*, 2007]. The spectral wavebands and wavelength ranges of the MODIS spectral albedo are specified in Table 1. We established the linear relationship between BBE and each spectral albedo, BBE, and seven spectral albedos, respectively. Figure 1 shows the scatterplot of BBE predicted by the fitted linear relationship between BBE and seven spectral albedos versus ASTER BBE as well as the histogram of the difference. The R^2 of the fitting is 0.831, the bias is 0.0002, and the root mean square error (RMSE) is 0.011. If only one spectral albedo was used in the fitting, the corresponding R^2 are 0.453, 0.405, 0.002, 0.197, 0.430, 0.454, and 0.610, respectively. We also tried fitting the relationship using the data ranging from November 2000 through January 2001 and the entire year 2002. Similar results were obtained. It is evident that the information provided by single spectral albedo is not enough for predicting BBE for bare soil. Predicting BBE with seven spectral albedos together may be an effective way that should be employed. If the NDVI threshold was increased to 0.2, the conclusion still holds true.

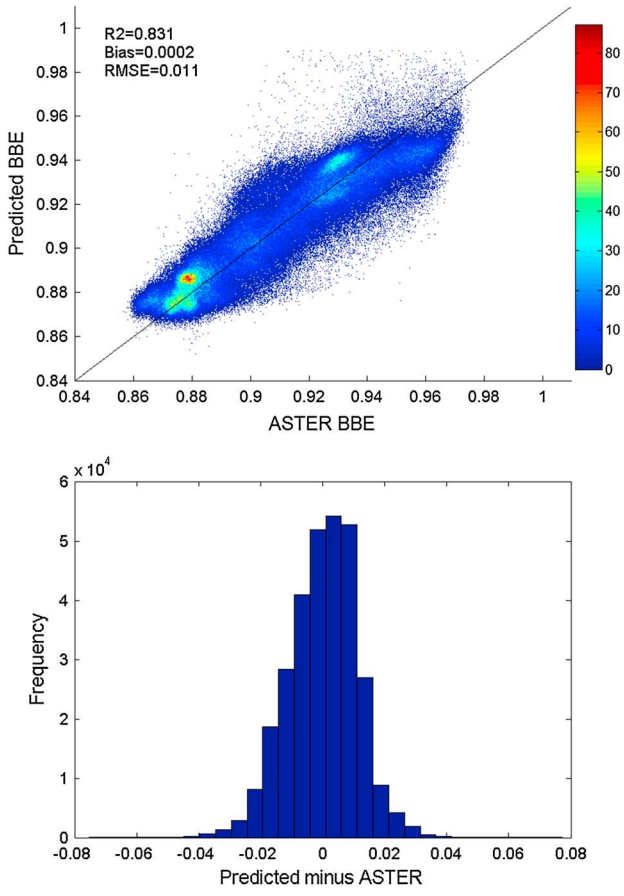

Figure 1. Comparison of BBE predicted by the fitted linear relationship between BBE and seven spectral albedos versus ASTER BBE as well as the histogram of the bias.

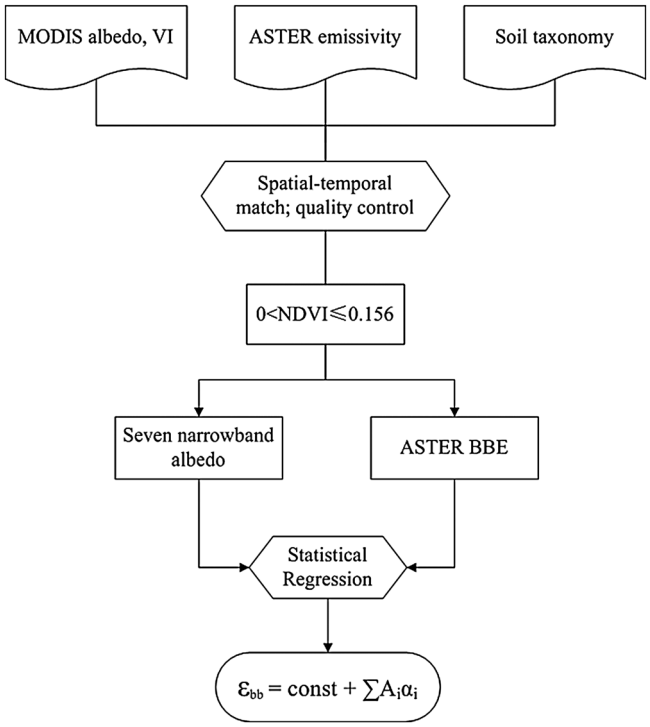

Figure 2. Flowchart for establishing the relationship between the MODIS spectral albedos and ASTER BBE.

2.2. Estimating BBE of Global Bare Soil

The scheme of our method is presented in Figure 2, where ε_{bb} is the broadband emissivity, α_i is the MODIS spectral albedo, and A_i is the regression coefficient. The input satellite data were (1) the MODIS albedo products (including the MODIS albedo product (MCD43B3) and its quality control (QC) data (MCD43B2)), (2) the MODIS NDVI product (MOD13A2), and (3) the ASTER emissivity product (AST05). The temporal and spatial resolutions of the MCD43B3 product were 8 days and 1 km, respectively. There are two types of albedo: white-sky (diffuse) and black-sky (direct). The seven spectral black-sky albedos were used in this study. MODIS NDVI was used to identify bare soil pixels. The temporal and spatial resolutions of the NDVI were 16 days and 1 km,

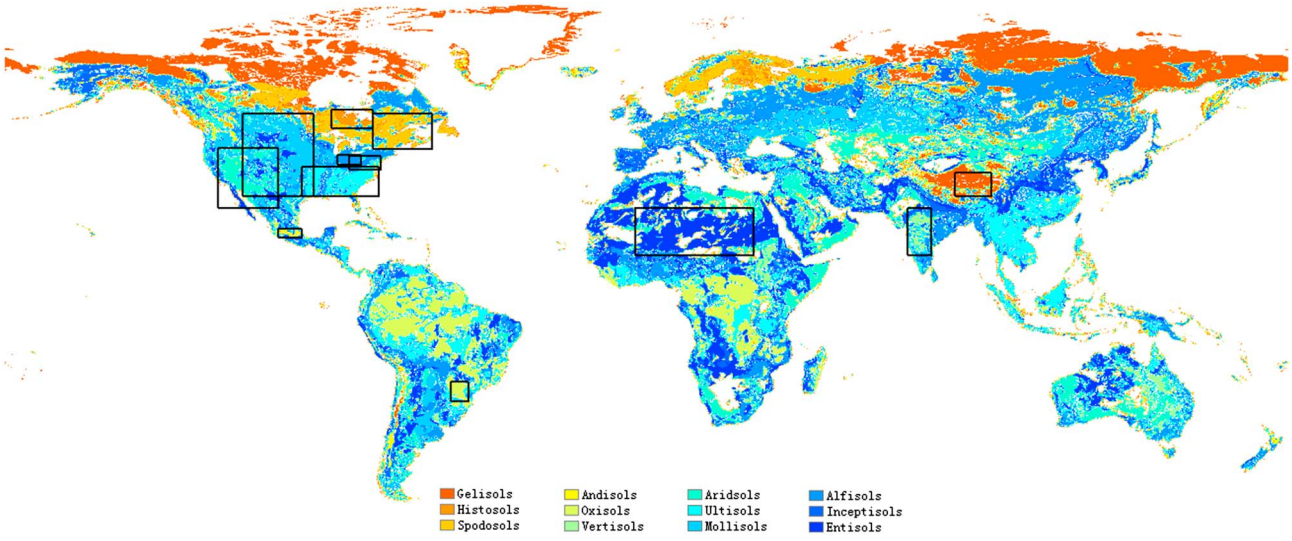

Figure 3. The U.S. Department of Agriculture Natural Resources Conservation Service soil taxonomy and selected experiment areas. Other classes such as rocky land, shifting sand, and ice/glacier are not included in the map.

Table 2. Geographical Locations of Selected Study Areas and Time Intervals for the Used Data

Soil Order	(Latitude; Longitude)	Time Interval
Alf sols	(38.67° to 41.77°; −86.7° to −80.03°)	2009.01–2009.03; 2007.01–2007.03
Andisols	(18.3° to 20.7°; −103.3° to −96.7°)	2009.02–2009.03; 2008.01–2008.03
Aridisols	(26.7° to 43.4°; −120° to −103.3°)	2009.01–2009.02; 2008.01–2008.03
Entisols	(13.3° to 26.7°; −3.3° to 30°)	2009.02–2009.02; 2008.01–2008.02
Gelisols	(30.03° to 36.7°; 86.63° to 96.63°)	2008.01–2008.01; 2009.01–2009.04
Inceptisols	(30.03° to 36.7°; 86.63° to 96.63°)	2008.01–2008.01; 2009.01–2009.04
Mollisols	(30° to 53.4°; −113.3° to −93.4°)	2009.03–2009.03; 2008.01–2008.03
Oxisols	(−27.5° to −22°; −55° to −50°)	2008.07–2008.09; 2009.01–2010.01
Ultisols	(30° to 38.4°; −96.7° to −75°)	2008.10–2009.02; 2007.01–2007.04
Vertisols	(13.3° to 26.7°; 73.3° to 80°)	2009.02–2009.03; 2008.01–2008.03

respectively. The requisite auxiliary data were the soil taxonomy, which is a basic system of soil classification for making and interpreting soil surveys. The soil taxonomy used in this study is based on a reclassification of the 1994 Food and Agriculture Organization-United Nations Educational, Scientific and Cultural Organization soil map of the world combined with a soil climate map (http://soils.usda.gov/use/worldsoils/mapindex/order.html). There were 12 soil orders in the map (Figure 3). The map's spatial resolution was approximately 0.0333°, with 5400×10,800 pixels. According to the soil taxonomy, we selected study areas for each soil order. To extract as many bare soil pixels as possible, we selected a relatively large and homogeneous region as the study area for each soil order. For some minor soil orders such as histosols and spodosols, we tested several areas and time intervals but found no bare soil pixels. We found it difficult to locate bare soil pixels at high latitudes and equatorial zones. The selected study areas are shown in Figure 3. Table 2 provides the detailed geographical locations of the selected study areas for each soil order and the time intervals for the data used. The ASTER and MODIS data were matched temporally based on the ASTER overpass time and the production period of the MODIS albedo product. The Universal Transverse Mercator projection of the ASTER emissivity product and the sinusoidal projection of the MODIS albedo product were transformed into the geographical projection. The ASTER 90 m emissivity product was aggregated to 1 km by averaging the values of ASTER pixels that fell into the MODIS 1 km pixel, thereby matching the spatial resolution of the MODIS albedo. High-quality and clear-sky data were extracted based on their respective QC data. The NDVI threshold was set to 0.156 to discriminate bare soil pixels, based on a previous work [*Momeni and Saradjian*, 2007]. If the NDVI was >0 and ≤0.156, the pixel was labeled as bare soil. A pixel was specified as vegetated pixel when the NDVI was >0.156. After spatiotemporal matching and bare soil pixel identification, we obtained the seven MODIS spectral albedos and five ASTER narrowband emissivities for a certain soil order. The ASTER narrowband emissivities were converted into BBE using a linear formula. Several formulae can be used to calculate the BBE in different spectral domains using satellite narrowband emissivities [*Liang*, 2004; *Ogawa et al*., 2008; *Peres and DaCamara*, 2006; *Tang et al*., 2011; *Wang et al*., 2005]. Using the simulated emissivity spectra with a spectral range of approximately 1–200 μm, Cheng et al. investigated the accuracy of BBE in different spectral regions when estimating surface longwave net radiation [*Cheng et al*., 2013]. They suggested that the surface longwave net radiation in the 1–200 μm spectral range can replace all-wavelength surface longwave net radiation, and the BBE in the 8–13.5 μm spectral range is the most appropriate for calculating land surface longwave net radiation in the 1–200 μm spectral range. The linear formulae for converting narrowband emissivities to BBE in the 8–13.5 μm spectral range for ASTER and MODIS were derived using 424 emissivity spectra (240 from the ASTER spectral library, i.e., http://speclib.jpl.nasa.gov/, 109 from the MODIS The University of California, Santa Barbara (UCSB) spectral library, i.e., http://g.icess.ucsb.edu/modis/EMIS/html/em.html, and our 75 outdoor measured soil emissivity spectra), which included soil,

Table 3. ASTER and MODIS TIR Channels and Their Spectral Ranges[a]

Band	Spectral Range (μm)
ASTER	
B_{10}	8.125–8.475
B_{11}	8.475–8.825
B_{12}	8.925–9.275
B_{13}	10.25–10.95
B_{14}	10.95–11.65
MODIS	
B_{29}	8.40–8.70
B_{31}	10.78–11.28
B_{32}	11.77–12.27

[a]B_{10}–B_{14} represent the five ASTER TIR channels, and B_{29}–B_{32} denote the six MODIS TIR channels.

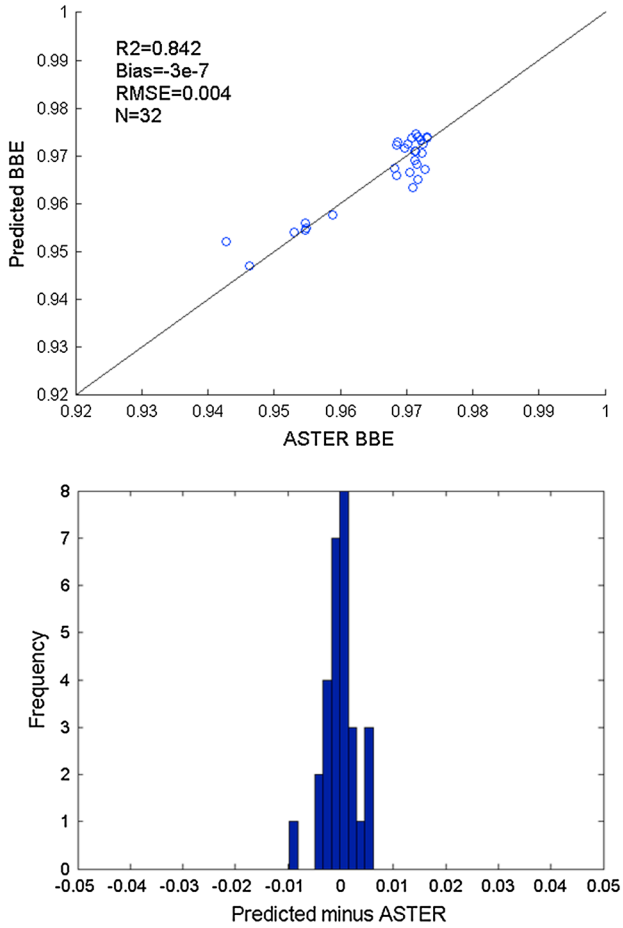

Figure 4. Comparison of ASTER BBE and that predicted by equation 3 from the derivation data for andisols in bare soil, as well as the histogram of the bias.

rock, vegetation, water, and snow/ice. Table 3 shows the TIR bands and their spectral ranges for ASTER and MODIS. The formulae are expressed as follows

$$\varepsilon_{bb\_ast} = 0.197 + 0.025\varepsilon_{10} + 0.057\varepsilon_{11} + 0.237\varepsilon_{12} + 0.333\varepsilon_{13} + 0.146\varepsilon_{14} \quad (1)$$

$$\varepsilon_{bb\_mod} = 0.095 + 0.329\varepsilon_{29} + 0.572\varepsilon_{31} \quad (2)$$

where ε_{bb_ast} is ASTER BBE, ε_{10}–ε_{14} are five ASTER narrowband emissivities, ε_{bb_mod} is MODIS BBE, while ε_{29} and ε_{31} are the MODIS narrowband emissivities for channels 29 and 31. The R^2 and RMSE for ASTER were 0.983 and 0.005, respectively. The R^2 and RMSE for MODIS were 0.932 and 0.010, respectively. Equation 2 was used to calculate the MODIS BBE in section 4.1. The extracted BBE-albedo pairs for each soil order were randomly split into two parts, 70% BBE-albedo pairs were used to derive a linear function of ASTER BBE in the form of seven MODIS spectral albedos by linear regression, and 30% BBE-albedo pairs were used for testing the derived linear function.

3. Results Analysis

3.1. Bare Soil

It is more desirable to derive one formula using all the extracted BBE-albedo pairs for two reasons: (1) the spatial resolution of the soil taxonomy is much coarser than that of the satellite data used, and (2) the accuracy of the soil taxonomy is relatively low. We derived one formula using all the extracted BBE-albedo pairs for bare soil. However, it did not work well for all soil orders combined. Thus, we derived three formulae, i.e., one formula for andisols, one formula for ultisols, and one formula for the remaining eight soil orders.

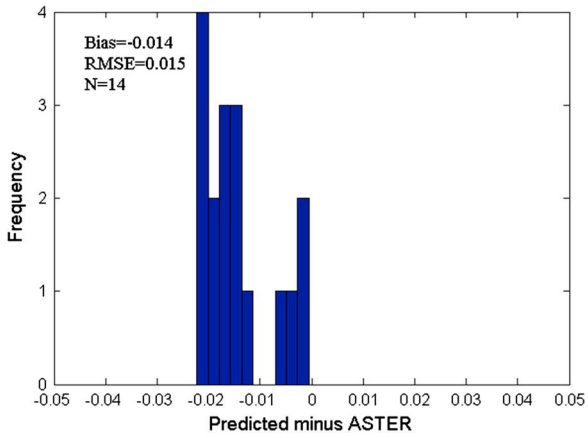

Figure 5. Difference histograms of ASTER BBE and that retrieved by equation (3) from the test data for andisols in bare soil.

Each formula and the coefficient for each variable were significantly below the confidence level of $P<0.05$. The formulae are expressed as follows

$$\varepsilon_{BB\_s1} = 0.963 + 0.643a_1 - 1.011a_3 - 0.137a_7 \quad (3)$$

$$\varepsilon_{BB\_s2} = 0.976 + 0.138a_1 + 0.040a_2 + 0.264a_3 - 0.383a_4 + 0.031a_6 - 0.124a_7 \quad (4)$$

$$\varepsilon_{BB\_s3} = 0.953 - 0.827a_1 + 0.447a_2 + 0.570a_3 - 0.041a_4 + 0.130a_5 + 0.006a_6 - 0.153a_7 \quad (5)$$

where ε_{BB_s1}, ε_{BB_s2}, and ε_{BB_s3} are the BBE for andisols, ultisols, and the remaining eight soil orders, respectively.

Figure4 shows the scatterplot for the BBE predicted using equation (3) versus the ASTER BBE for andisols and the histogram of the bias. The correlation was 0.842. The bias was centered on zero and distributed in a narrow band, but its value was very small and it can be neglected, while the RMSE was 0.004. The test result is

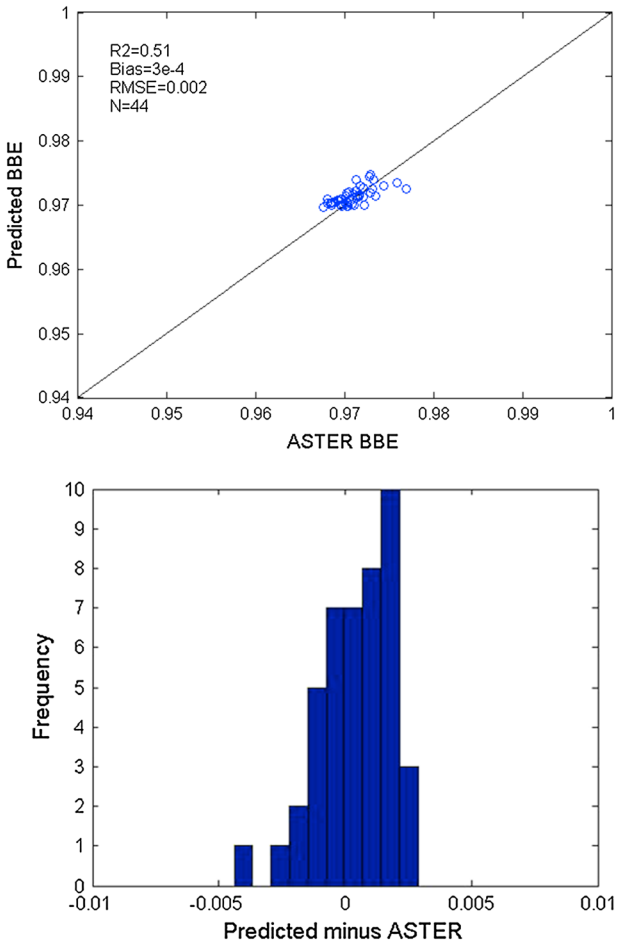

Figure 6. Comparison of ASTER BBE and that predicted by equation 4 from the derivation data for ultisols in bare soil, as well as the histogram of the bias.

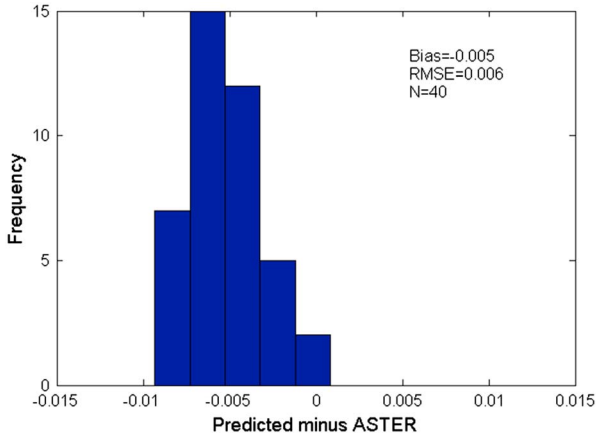

Figure 7. Difference histograms of ASTER BBE and that retrieved by equation (4) from the test data for ultisols in bare soil.

shown in Figure 5. The bias was as high as −0.014, and the RMSE was 0.015. The number of pixels used to establish and test equation (3) was quite limited, which might have made equation (3) more unstable and insufficiently representative. The test results may also have been affected by this problem. Figure 6 shows the scatterplot for the BBE predicted using equation (4) versus the ASTER BBE for the ultisols and the histogram of the bias. The correlation was slightly lower as 0.51, the bias was $3e^{-4}$, and the RMSE was 0.002. The test result is shown in Figure 7. The bias was −0.005 and the RMSE was 0.006. Figure 8 shows the scatterplot for the BBE predicted using equation (5) versus the ASTER BBE for eight soil orders and the histogram of the bias. The correlation was 0.799, the bias was −0.001, and the RMSE was 0.012. Table 4 shows the bias and RMSE for each of the eight soil orders. The absolute bias and RMSE were <0.008 and 0.019, respectively. The test result is shown in Figure 9. The bias was −0.001 and the RMSE was 0.013.

3.2. Transition Zone

In sparsely vegetated areas, it is hard to determine whether the pixels relate to bare soil or a vegetated surface. The BBE of such pixels was calculated using the formula for bare soil or a vegetated surface. Thus, the variation in the BBE for these pixels would be larger than the actual variation. This leads to step discontinuities when generating a global land surface BBE product. We propose to specify a transition zone to mitigate the BBE difference between the bare soil and vegetated pixels by using the NDVI and give a BBE estimation method for the transition zone. The BBE of the pixels located in the transition zone is the average of their affiliations, which depends on the NDVI of the pixels. In this study, pixels with an NDVI ranging from 0.1 to 0.2 were labeled as transition zone pixels. If the NDVI is between 0.1 and 0.156, its BBE is the average of that calculated using the formula for bare soil and the transition zone. If the NDVI lies between 0.156 and 0.2, its BBE is the average of that calculated using the formulae for the transition zone and vegetation.

Similar to the method used for bare soil, we first derived one formula for all soil orders. However, this method did not perform well for all soil orders combined. Thus, we derived three formulae, i.e., one formula for andisols, one formula for vertisols, and one formula for the remaining eight soil orders. Each formula and the coefficient for each variable were significantly below the confidence level of $P<0.05$. The formulae are expressed as follows:

$$\varepsilon_{BB\_t1} = 1.006 - 0.339a_2 + 0.142a_7 \quad (6)$$

$$\varepsilon_{BB\_t2} = 0.964 + 0.195a_1 + 0.256a_2 - 0.745a_3 + 0.099a_6 - 0.300a_7 \quad (7)$$

$$\varepsilon_{BB\_t3} = 0.954 - 0.782a_1 + 0.345a_2 + 0.776a_3 - 0.111a_4 + 0.056a_5 + 0.080a_6 - 0.131a_7 \quad (8)$$

where ε_{BB_t1}, ε_{BB_t2}, and ε_{BB_t3} are the BBEs for andisols, vertisols, and the remaining eight soil orders, respectively.

Figure 10 shows a scatterplot of the BBEs predicted using equation (6) versus the ASTER BBE for andisols and the histogram of the bias. The correlation was relatively low with a value of 0.48, while the bias and RMSE were $5e^{-8}$ and 0.008, respectively. The test result is presented in Figure 11. The bias and RMSE were 0.004 and 0.012, respectively. The scatterplot of the BBEs predicted using equation 7 versus the ASTER BBE for vertisols is shown in Figure 12. The correlation was 0.677, while the bias and RMSE were $1e^{-7}$ and 0.007, respectively. The test result is presented in Figure 13. The bias and RMSE were −0.002 and 0.009. The scatterplot of the BBEs predicted using equation 8 versus the ASTER BBE for the eight soil orders is shown in Figure 14, where the correlation was 0.804. The bias was 0.001 and the RMSE was 0.012. Table 5 shows the bias and RMSE for each of the eight soil orders. The absolute bias and RMSE were <0.008 and 0.016, respectively. The test result is shown in Figure 15. The bias was 0.003 and the RMSE was 0.013.

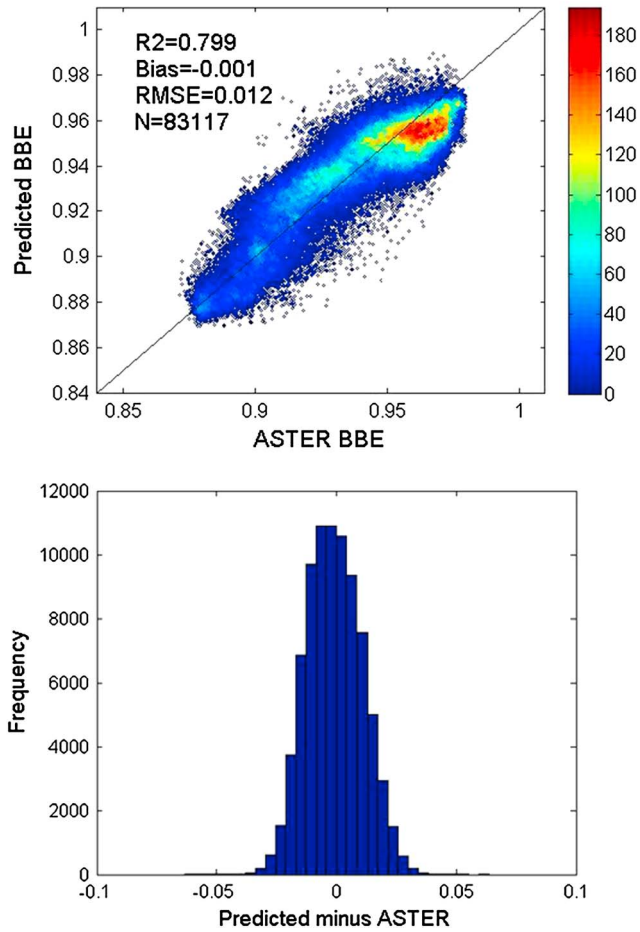

Figure 8. Comparison of ASTER BBE and that predicted by equation (5) from the derivation data for the remaining eight soil orders in bare soil, as well as the histogram of the bias.

3.3. Error Analysis

The accuracy of the estimated BBE was determined by the accuracy of MODIS spectral albedos and the accuracy of regression together. We can calculate the absolute accuracy of estimated BBE with the formula below

$$\varepsilon = \sqrt{\mathrm{RMSE}^2 + \Sigma {A_i}^2 \cdot {\sigma_i}^2} \tag{9}$$

where ε is the BBE accuracy, A_i is the coefficient in equations (3)–(8), and σ_i is the accuracy of MODIS spectral albedo. According to the validations of the MODIS albedo product [*Cescatti et al.*, 2012; *Liang et al.*, 2002; *Román et al.*, 2009; *Wang et al.*, 2004; *Wang et al.*, 2012], we assigned 0.01 as the average accuracy of MODIS spectral albedo for vegetated area and 0.02 as the value for bare soil. Assuming the accuracy of the MODIS spectral albedo is 0.01, the accuracy of BBE estimation with equations (3)–(8) were 0.013, 0.005, 0.016, 0.009, 0.011, and 0.017, respectively. If the accuracy of the MODIS spectral albedo was reduced to 0.02, the accuracy of BBE estimation with equations (3)–(8) were 0.024, 0.010, 0.025, 0.011, 0.019, and 0.026, respectively.

Table 4. Bias and RMSE for Each of the Eight Soil Orders in Bare Soils

Soil Order	Alfisols	Aridisols	Entisols	Gelisols	Inceptisols	Mollisols	Oxisols	Vertisols
Sample number	34	12,547	33,025	34,009	513	2821	11	157
Bias	0.004	−0.002	0.002	−0.003	−0.008	−0.006	−0.004	−0.001
RMSE	0.010	0.011	0.011	0.012	0.019	0.009	0.016	0.008

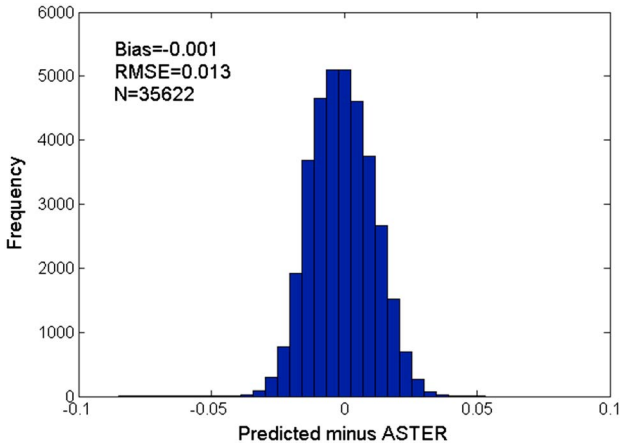

Figure 9. Difference histograms of ASTER BBE and that retrieved by equation (5) from the test data for the remaining eight soil orders in bare soil.

A Monte Carlo (MC)-based uncertainty and sensitivity analysis software SimLab was used to conduct uncertainty and sensitivity analysis. MC-based uncertainty and sensitivity analyses are based on performing multiple model evaluations with probabilistically selected model input and then using the results of these evaluations to determine (1) the uncertainty in model predictions and (2) the input variables that gave rise to this uncertainty. In this study, a global sensitivity analysis method Fourier amplitude sensitivity test (FAST) was used for sampling and sensitivity analysis [*Saltelli et al.*, 1999]. FAST approach is based on performing numerical calculations to obtain the expected value and variance of a model prediction. The basis of this calculation is a transformation that converts a multidimensional integral over all the uncertain model inputs to a one-dimensional integral. The

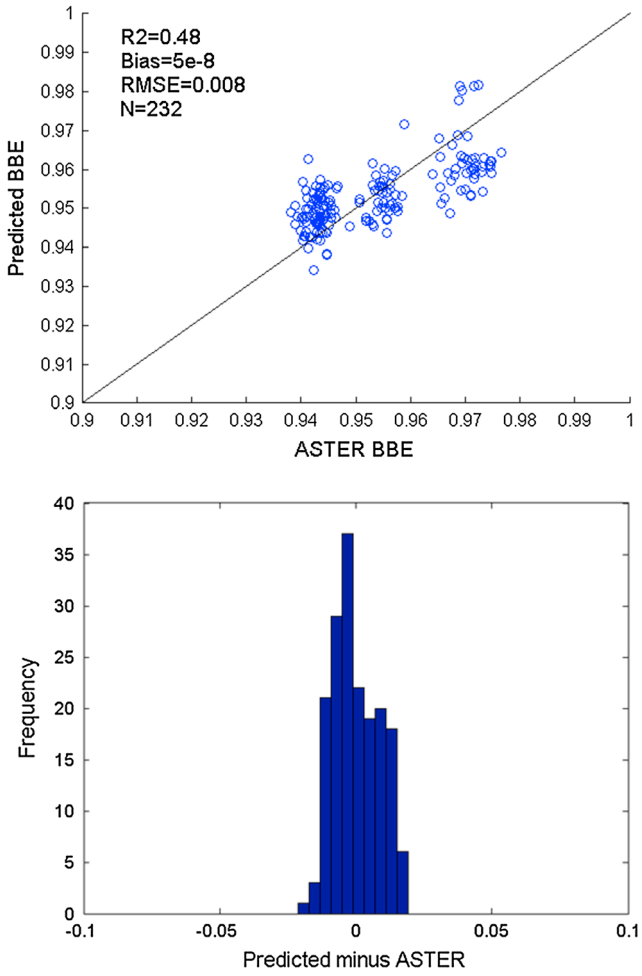

Figure 10. Comparison of ASTER BBE and that predicted by equation 6 from the derivation data for andisols in the transition zone, as well as the histogram of the bias.

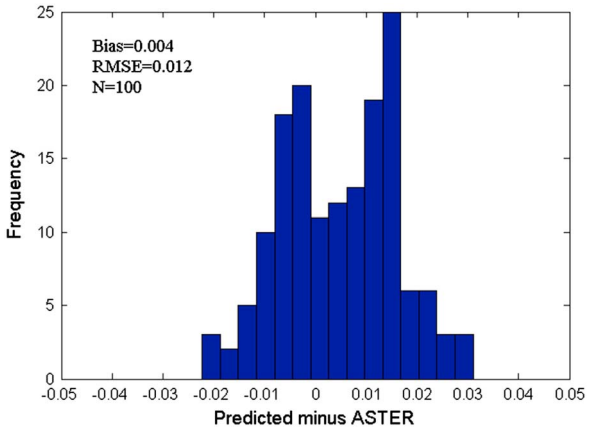

Figure 11. Difference histograms of ASTER BBE and that retrieved by equation (6) from the test data for andisols in the transition zone.

FAST sensitivity indices of the first order are calculated using the terms in the Fourier decomposition of the model output. Provided with the probability distribution function of each input, we generated a large number of samples with FAST sampling technique and then used FAST to perform sensitivity analysis for equations (3)–(8). The result was presented in Table6. We can see clearly from Table6 that the contribution of each input to the total variance is different. For example, the most evident result is that the most important factor is B1 in equation (3) that captures 71.4% of the output variance.

4. Validation

4.1. Comparison With the MODIS Product

According to the validation of different versions of the MODIS Land Surface Temperature and Emissivity (LST&E) using laboratory-measured sand emissivities, the V4.1 emissivity product is the best, whereas the V5

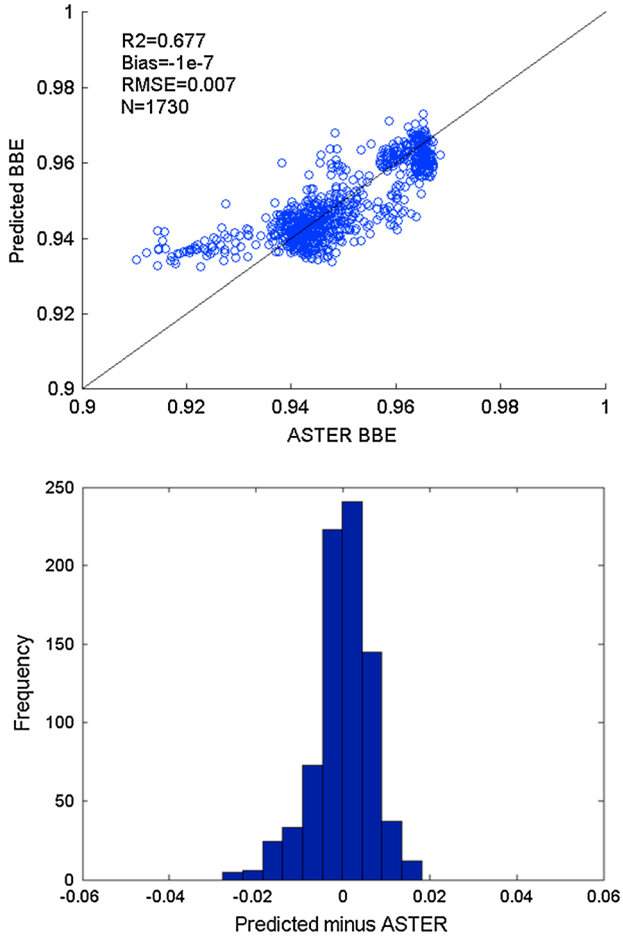

Figure 12. Comparison of ASTER BBE and that predicted by equation 7 from the derivation data for vertisols in the transition zone, as well as the histogram of the bias.

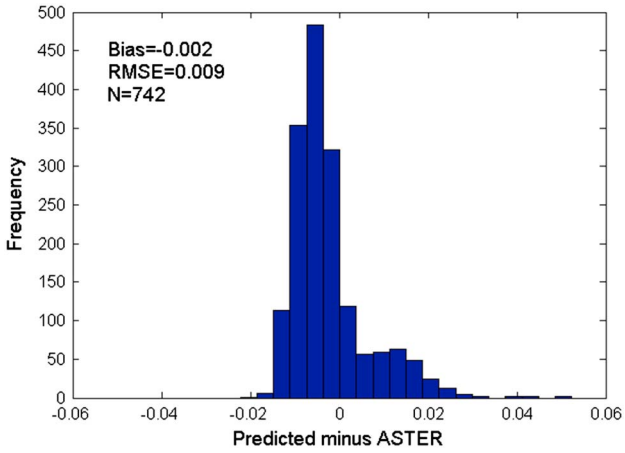

Figure 13. Difference histograms of ASTER BBE and that retrieved by equation (7) from the test data for vertisols in the transition zone.

emissivity product is the worst [*Hulley and Hook*, 2009]. We compared the estimated BBE with the BBE derived from MOD11B1 LST&E products (Versions 4.1 and 5). The MOD11B1 LST&E products (Versions 4.1 and 5) were daily 5 km and 6 km products in a sinusoidal projection. They were retrieved using a day/night algorithm from the coregistered day and night image pair [*Wan and Li*, 1997]. To collect as many bare soil pixels as possible, the study areas we selected for the four soil orders (aridisols, entisols, gelisols, and mollisols) corresponded to large numbers of bare soil pixels as the study areas in this section. The time intervals of data were the same as those used in section 3. First, the 8 day MODIS BBE was developed in the following two steps. (1) *Derive the 8 day narrowband emissivity*. The 8 day narrowband emissivity was derived by aggregating the daily emissivity products. (2) *Calculate the 8 day MODIS BBE*. We calculated the MODIS BBE in the 8–13.5 spectral ranges using equation (2) from three combined 8 day narrowband emissivities. Second, we aggregated the 1 km BBE

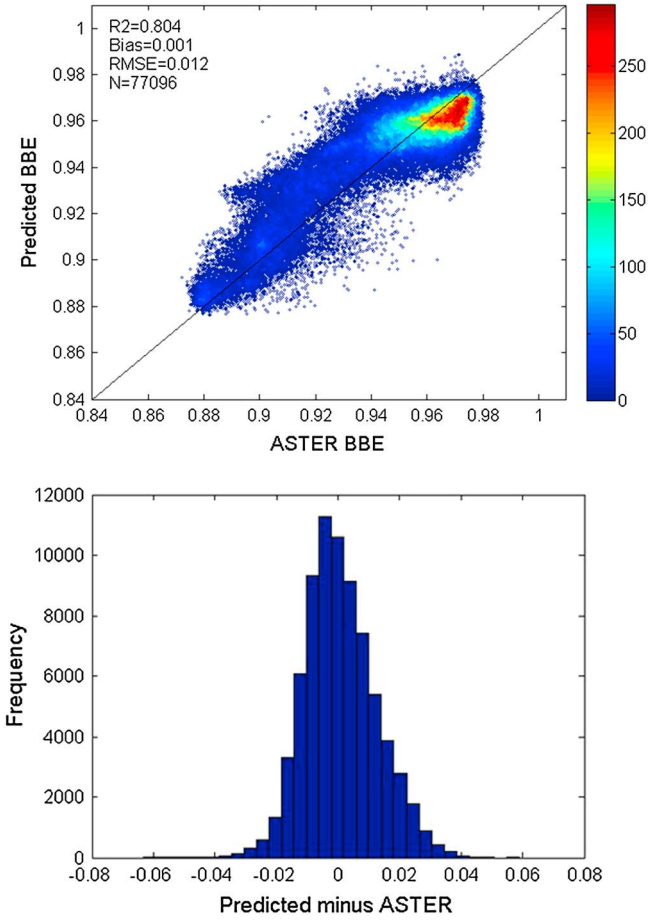

Figure 14. Comparison of ASTER BBE and that predicted by equation 8 from the derivation data for the remaining eight soil orders in the transition zone, as well as the histogram of the bias.

Table 5. Bias and RMSE for Each of the Eight Soil Orders in Transition Zones

Soil Order	Alfisols	Aridisols	Entisols	Gelisols	Inceptisols	Mollisols	Oxisols	Vertisols
Sample number	75	22,927	19,977	26,013	944	5418	12	1730
Bias	0.008	−0.002	0.007	−0.001	0.005	−0.008	0.008	0.004
RMSE	0.012	0.010	0.015	0.010	0.016	0.014	0.010	0.007

estimated using the new algorithm into 5 km and 6 km, respectively. Finally, we compared the MODIS BBE with the estimated BBE. The results are shown in Figures 16 and 17. The MODIS BBE derived from the Version 5 emissivity product was larger than the estimated BBE, which was similar to a previous result [*Wang and Liang*, 2009]. The biases were −0.008 and −0.010, and the RMSEs were 0.026 and 0.023 for the bare soil and transition zone, respectively. The MODIS BBE derived from the Version 4.1 emissivity product was less than the estimated BBE, and the biases were 0.001 and 0.003, while the RMSEs were 0.015 and 0.013 for the bare soil and transition zone, respectively. We also compared the estimated BBE with the ASTER BBE for these four soil orders. The estimated BBE was in good agreement with the ASTER BBE, i.e., the biases were −0.001 and 0.001, while the RMSEs were 0.012 and 0.011 for the bare soil and transition zone, respectively. Thus, we can draw two conclusions based on a comparison of the results. The first is that the BBE derived from the different versions of the MODIS emissivity product were inconsistent. The second is that the accuracy of the estimated BBE is better than that derived from MODIS emissivity products.

4.2. Validation Using In Situ Measurements

Field trials are of vital importance for validating or testing the algorithms developed to retrieve specific biogeophysical parameters from satellite or aircraft data [*Liang et al*., 2002; *Sobrino et al*., 2006], which is also helpful to improve the designed algorithm. We collected field-measured emissivity over large homogeneous surfaces from three field trials conducted in China during the past 6 years [*Dong et al*., 2013; *Zhang et al*., 2009]. These emissivity data were used to validate this new algorithm. The first field trial was carried out on 18 August 2006 at the Dunhuang Calibration Site in China for the radiometric calibration of domestic satellites. A field measurement radiometer (CIMEL CE312-1) and an Infragold board were used to determine the emissivity of the Gobi Desert surface. The CIMEL CE312-1 was initially calibrated using a thermal infrared blackbody at five known temperatures, while the radiation of the target and environment were measured alternately. The measurements were repeated five times. The narrowband emissivity was determined using the ASTER temperature and emissivity separatio (TES) algorithm [*Gillespie et al*., 1998]. Following the same method documented in section 2, we derived the formula for converting the CE312 narrowband emissivities to BBE at 8–13.5 μm. The average BBE was 0.945, while the BBE calculated using the new algorithm was 0.946. Thus, the difference was 0.001. The second field trials were carried out on 31 July and 12 October 2007 at the Dunhuang Calibration Site in China. A Bomem MR 154 Fourier transform infrared (FTIR) spectrometer and a Labsphere gold plate were used to measure the spectral radiance emitted by the Gobi Desert surface and the environment. The measurements were repeated 10 times for each target. The emissivity spectrum was derived from the radiometric measurements using the iterative spectrally smooth temperature and emissivity separation (ISSTES) algorithm [*Borel*, 2008]. The measured emissivity spectra were converted to the BBE at 8–13.5 μm. The average BBE measurements were 0.927 and 0.923, respectively. The estimated BBEs were 0.947 and 0.945, respectively. Thus, the average difference was 0.021. The final field trial was conducted on 6 June 2011 in the Taklimakan Desert, XinJiang Province, China, which is the largest active desert in China and the second largest in the world. A Model 102 Portable Field Spectrometer and a

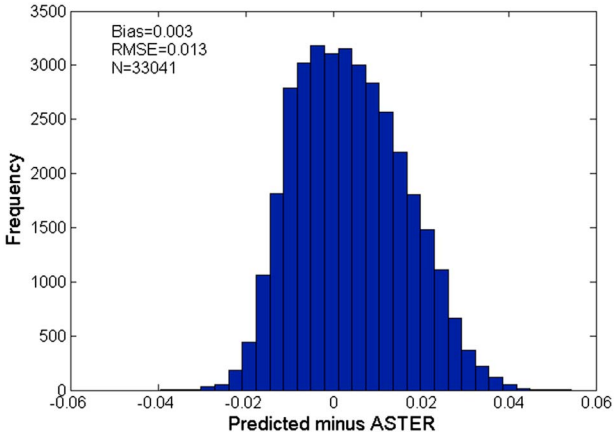

Figure 15. Difference histograms of ASTER BBE and that retrieved by equation (8) from the test data for the remaining eight soil orders in the transition zone.

Table 6. FAST Calculated Model Uncertainty for Equations (3)–(8), as Well as the FAST Sensitivity Indices of the First Order for Each Input in Equations (3)–(8)[a]

	Uncertainty		FAST Sensitivity Indices of the First Order						
Equation	Mean	Standard	B1	B2	B3	B4	B5	B6	B7
3	0.968	0.023	0.714	-	0.058	-	-	-	0.197
4	0.960	0.013	0.104	0.018	0.012	0.276	-	0.031	0.486
5	0.942	0.035	0.501	0.304	0.008	0.001	0.055	0.001	0.104
6	0.968	0.026	-	0.814	0.002	-	-	-	0.131
7	0.952	0.030	0.095	0.338	0.015	-	-	0.053	0.428
8	0.955	0.040	0.639	0.261	0.006	0.003	0.006	0.015	0.034

[a]B1–B7 denote MODIS seven spectral albedo bands.

Labsphere gold plate were used to measure the spectral radiance emitted by the target and the environment. The emissivity spectrum was derived from the radiometric measurements using the ISSTES algorithm [*Borel*, 2008]. We selected two relatively homogeneous sites in the center of the Taklimakan Desert. We conducted three measurements at each site and then randomly selected three points within a distance of approximately 500 m from the site where we conducted three measurements at each point. The 12 emissivity spectra were averaged and regarded as the measured emissivity of the site. The average

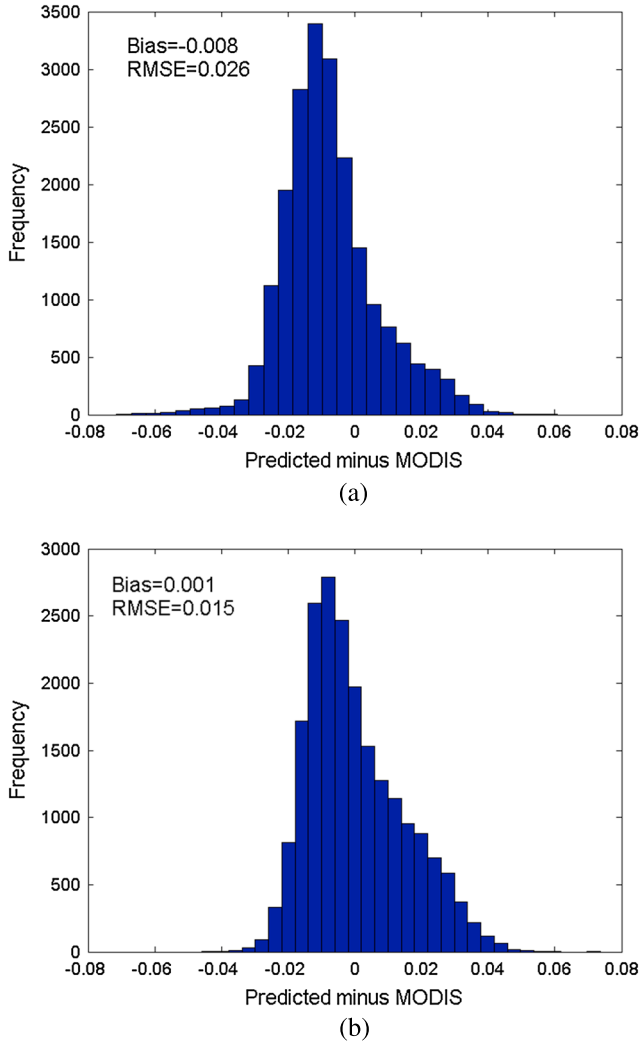

Figure 16. Difference histograms of MODIS BBE and that estimated using the new algorithm for bare soil. (a) Version 5; (b) Version 4.1.

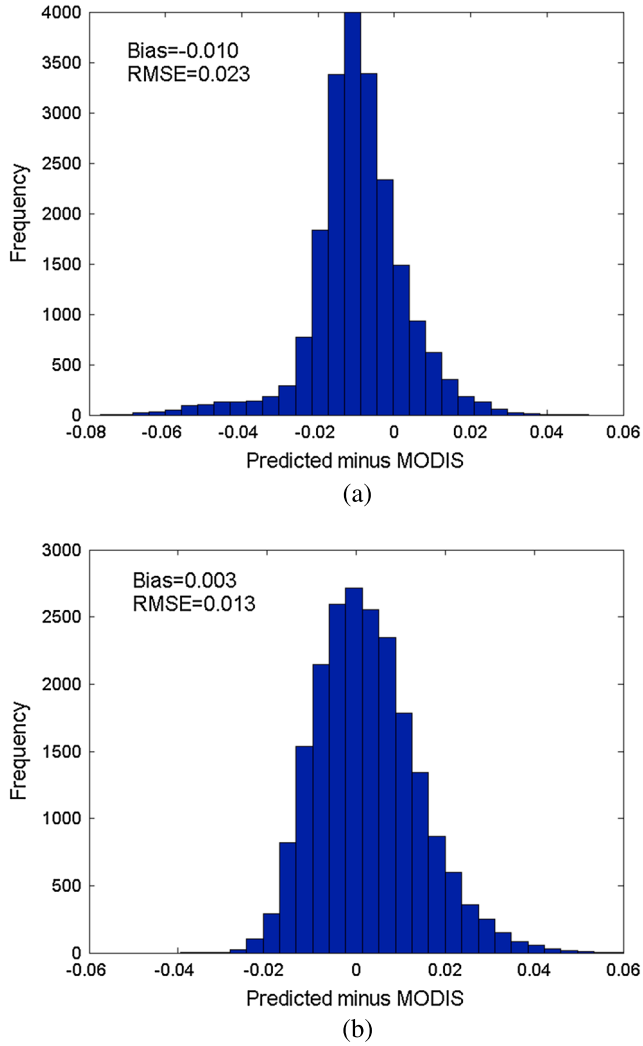

Figure 17. Difference histograms of MODIS BBE and that estimated using the new algorithm for the transition zone. (a) Version 5; (b) Version 4.1.

emissivity spectra were converted into the BBEs at 8–13.5 μm. The measured BBEs were 0.915 and 0.913, whereas the BBEs estimated using the new algorithm were 0.928 and 0.929, respectively. Thus, the average difference was 0.015. According to the results of three field trials, the average difference between the estimated BBE and the measured BBE was 0.015.

Hulley and Hook conducted five separate field trials to collect sand samples from nine sand dunes during the spring and early summer of 2008 to validate the North American ASTER Land Surface Emissivity Database [*Hulley et al*., 2009]. The emissivity spectra of the samples was measured in a laboratory using a Nicolet 520 FTIR spectrometer equipped with a Labsphere integrating sphere [*Baldridge et al*., 2009]. The corresponding ASTER narrowband emissivities were derived by convolving the laboratory-measured emissivity spectra with the ASTER TIR spectral response functions. The mineralogy of each dune site was also measured using the X-ray diffraction method. Further details on the dune sites can be found in the published paper. Five relatively large and homogeneous dune sites were selected to validate this new algorithm. The spatially matched ASTER emissivity product and MODIS albedo product were also downloaded for the period from March 2008 to June 2008. Overall, we acquired 9 ASTER images for Algodones and Great Sands, 8 ASTER images for Kelso and Little Sahara, and 10 ASTER images for Stovepipe Wells. For each dune site, we converted the derived narrowband emissivity and downloaded ASTER narrowband emissivity to BBEs in the 8–13.5 μm spectral range using equation (2) and compared the values with those calculated using the new algorithm. Table 7 shows the difference between the estimated BBE and the measured BBE, and that between the retrieved BBE

Table 7. BBE Difference Between the Retrieved BBE and Field-Measured BBE as Well as That Between the Retrieved BBE and ASTER BBE

Dune Sites	Field	ASTER	Retrieved	Retrieved-Field	Retrieved-ASTER
Algodones	0.906	0.900	0.920	0.014	0.020
Great Sands	0.924	0.946	0.946	0.021	0.000
Kelso	0.907	-	0.935	0.028	-
Little Sahara	0.914	0.945	0.942	0.028	−0.003
Stovepipe Wells	0.936	0.930	0.935	−0.001	0.005

and ASTER BBE. The estimated BBE agreed well with the ASTER BBE. The difference was 0.005. This result was consistent with the comparison results for bare soil shown in section 3.1. The difference between the estimated BBE and the measured BBE was 0.018. When combined with the validation results from field measurements in China, the average difference between the estimated BBE and the measured BBE was 0.016.

5. Generating Global Land Surface BBE Product

The data required to generate the global land surface BBEs were the MODIS reflectance data (MOD09A1), MODIS albedo products (MCD43B3 and MCD43B2), and soil taxonomy. The MODIS data were all processed by another group in our team to ensure good data quality. Processing included cloud clearing, spatiotemporal filtering, and gap filling. The 8 day 500 m MOD09A1 was aggregated into 1 km and used to calculate the 1 km NDVI. The water and snow/ice pixels were identified based on flags of the aggregated data. The 1 km NDVI was used to determine other land surface types. Overall, the land surface was divided into six types: water, snow/ice, bare soil ($0 < \mathrm{NDVI} \le 0.1$), soil transition zone ($0.1 < \mathrm{NDVI} \le 0.156$), vegetation transition zone ($0.156 < \mathrm{NDVI} < 0.2$), and vegetated area ($\mathrm{NDVI} \ge 0.2$) for the generation of the global land surface BBE. We used different methods to determine their BBEs. Equations (3)–(5) were used to calculate the BBE for bare soil, and equations (6)–(8) were used to calculate the BBE for the transition zone. The method for estimating the BBE for vegetated areas is described in a separate paper [*Ren et al*., 2013]. Equations (3)–(5) and the method for vegetated areas were used to calculate the BBEs for the soil transition zone, and equations (6)–(8) and the method for vegetated areas were used to calculate the BBEs for the vegetation transition zone. The emissivity spectrum of water can be simulated using the Fresnel equation, given its refractive index. Figure 18 shows the simulated pure water emissivity spectra together with the emissivity spectra in the ASTER spectral library and the MODIS UCSB spectral library. The measured emissivity spectra were distributed in a narrow band, which agree well with the simulated emissivity spectrum. The BBE of water in the ASTER spectral library was 0.984 for all three samples, while the value in the MODIS UCSB spectral library was 0.985 for all five samples. The BBE of water was specified as 0.985 during the production of the global land surface BBE. For snow and ice, we used the radiative transfer model and Fresnel equation, respectively, to simulate their emissivity spectra [*Cheng et al*., 2010b]. However, it was impractical to obtain the model inputs (snow effective radius and the refractive indices of snow and ice) on a global scale. Moreover, the emissivity spectra of snow/ice were angle dependent, and this dependency cannot be well simulated by radiative transfer models [*Cheng et al*., 2010b; *Hori et al*., 2006]. We

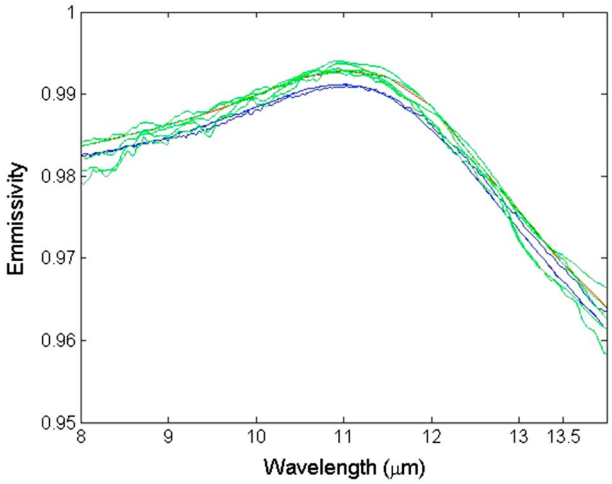

Figure 18. Comparison of simulated pure water emissivity (red), water emissivity spectra in the ASTER spectral library (blue), and water emissivity spectra in the MODIS UCSB emissivity spectra library (green).

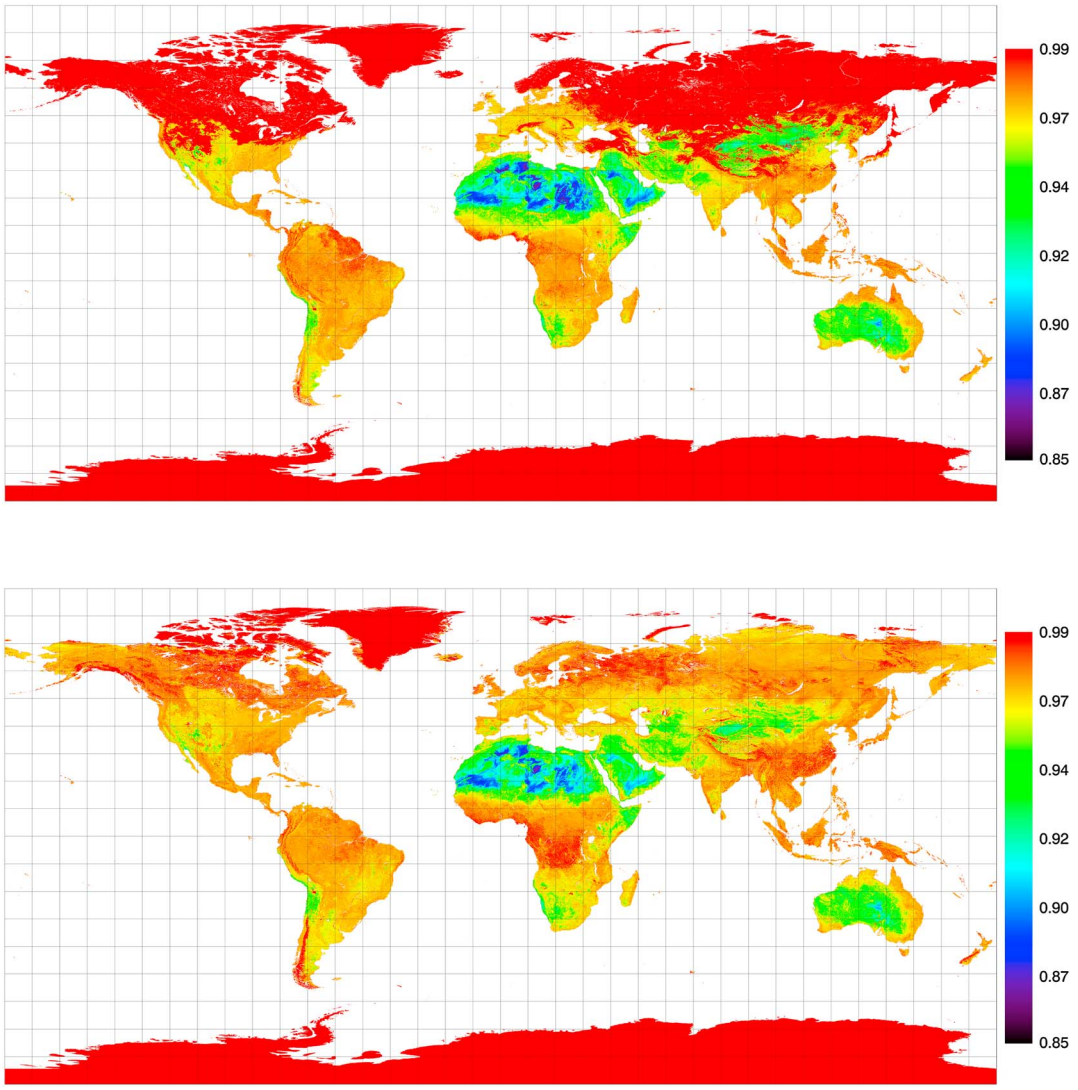

Figure 19. Global land surface BBE in Julian day (top) 49 and (bottom) 241 in 2008.

calculated the BBE of snow/ice using the emissivity spectra in the ASTER spectral library and the MODIS UCSB spectral library, and 0.985 was used as their BBE. The error was less than 0.005 when the viewing angle was less than 45°. Figure 19 shows an example of the estimated 8 day 1 km global land surface BBE in 2008. This product was released to the public on November 2012 along with other products [*Liang et al*., 2013; *Cheng et al*., 2014] and can be ordered from the Beijing Normal University (BNU) Center for Global Change Data Processing and Analysis (http://www.bnu-datacenter.com) and Global Land Cover Facility (http://glcf.umd.edu).

6. Discussion

Similar to the NDVI threshold method [*Sobrino et al*., 2008; *Valor and Caselles*, 1996], this new algorithm is a statistics-based algorithm. Though the remote-sensing community prefers to develop and use physical-based algorithms, a statistics-based algorithm is essentially useful for some specific applications. For example, we could not derive land surface temperature from a single-band thermal infrared sensor like Thematic Mapper (TM) without the help of the NDVI threshold method for determining land surface emissivity in advance. This is also the case for estimates of global 8 day 1 km land surface BBE for bare soil in this study as described in section 1.

The new algorithm has the usual merits of this type of algorithm such as simplicity, wide applicability, and acceptable accuracy. However, it also has an unavoidable drawback. This algorithm loses efficacy if the inputs deviate greatly from the general behavior of samples used to establish the algorithm. This algorithm also has the following weaknesses. (1) The difficulties of finding bare soil pixels at a 1 km spatial resolution with some minor soil orders means that the extracted BBE-albedo pairs were limited. Thus, the formula might not be representative even if the established formula can pass the confidence test. The results were greatly improved for soil orders with a high number of bare soil pixels, as shown in the test results for the derived formula presented in section 3.1. (2) The spatial resolution of the soil taxonomy was approximately 0.033°, which was inconsistent with the 1 km spatial resolution of the MODIS products used and the resized ASTER emissivity product. In addition, the errors in soil order classification may affect the established relationship for each soil order. In order to avoid classification errors, we aimed to derive one formula to represent the relationship between the BBE and albedo for the bare soil and transition zone. Unfortunately, we could not obtain an acceptable result for a few minor soil orders. We will incorporate finer soil taxonomy data when they are available.

Significant relationships were derived between ASTER BBE and MODIS albedos, which enabled the better accuracy of BBE retrieval, because both ASTER emissivity and MODIS albedo products are the best in the remote-sensing community [*Cescatti et al*., 2012; *Gillespie et al*., 2011; *Gillespie et al*., 1998; *Román et al*., 2009; *Schaaf et al*., 2002; *Wang et al*., 2012]. Furthermore, the BBE is formulated as a linear function of seven MODIS narrowband albedos rather than a single MODIS albedo in the study of *Zhou et al*. [2003a]. More bands bring more information content and will certainly improve the overall fitting accuracy. As shown in section 3.1, good agreement was found between this new BBE and the ASTER BBE calculated based on the ASTER emissivity for the bare soil and transition zone. Moreover, the new BBE also agreed well with the BBEs derived from field-measured BBEs, as shown in section 4.2. Thus, this new BBE has a comparable accuracy with that of ASTER BBE for bare soil and transition zone. The advantage of this new algorithm over the method of converting ASTER narrowband emissivities is obvious for global land surface BBE mapping. The scanning range of ASTER is narrow, while its revisit cycle is 16 days, which makes it almost impossible to produce a global land surface emissivity product on a monthly scale. The BBEs derived from different versions of the MODIS emissivity product were inconsistent. The MODIS BBE derived from the Version 5 emissivity product was higher than the estimated BBE, and the bias was on the order of 0.010. The MODIS BBE derived from the Version 4.1 emissivity product was less than the estimated BBE, and the bias was <0.003. The estimated BBE was in good agreement with the ASTER BBE, so the accuracy of the estimated BBE is higher than that derived from the MODIS emissivity products. Generally, this conclusion can be attributed to two aspects: (1) good performance of our proposed method and (2) the poor accuracy of the MODIS BBE in contrast. MODIS narrowband emissivities are determined by solving 14 variables in 14 equations [*Wan and Li*, 1997], which makes them prone to measurement noise and which may lead to local convergence [*Gillespie et al*., 1998; *Peres and DaCamara*, 2006]. Moreover, the conversion formula also contains error. For example, the RMSE of the conversion formula for MODIS was 0.010 in this study. In addition, this new BBE possesses two merits compared with the BBE calculated from MODIS narrowband emissivities retrieved from the day/night algorithm, as follows. The first is *high spatial resolution*. The spatial resolution of the new BBE is 1 km, whereas the BBE calculated from the MODIS emissivity product has a resolution of approximately 5 km. The second is *product availability*. The MODIS day/night algorithm requires clear-sky conditions during the day and night [*Wan and Li*, 1997]. This is a strict requirement and results in many gaps in the retrieved emissivity products.

7. Conclusions

In this study, we developed a new algorithm for estimating the global bare soil BBEs from the MODIS albedo. The algorithm combined the advantages of ASTER emissivity and MODIS albedo products and established the linear relationship between ASTER BBE and seven MODIS spectral albedos for bare soil. In order to mitigate step discontinuities in the global land surface BBE product, a transition zone was established, and so does the BBE estimation method for transition zone. Three linear formulae (equations (3)–(5)) were derived from the extracted BBE-albedo pairs for bare soil using a statistical regression method. We also obtained three linear formulae (equations (6)–(8)) for the transition zones using the same method as that used for bare soil. These equations and the coefficient for each variable were significantly below the confidence level of $P<0.05$. For bare soil, the correlation ranged from 0.51 to 0.842, and the bias and RMSE were less than 0.001

and 0.012, respectively. Regarding transition zone, the correlation ranged from 0.48 to 0.804, and the bias RMSE were less than 0.001 and 0.012, respectively. The test results indicated that the absolute bias and RMSE values for bare soil were less than 0.005 and 0.013 with the exception of andisols, and the absolute bias and RMSE values for the transition zone were less than 0.004 and 0.012. Given the accuracy of 0.01 for MODIS spectral albedo, the accuracy of BBE retrieval is better than 0.017.

The performance of the algorithm was evaluated initially by comparing the BBEs estimated using our algorithm with those calculated from the MODIS Version 4.1 and 5 LST&E products. The MODIS BBE derived from the Version 5 emissivity product was higher than the estimated BBE, with bias on the order of 0.01, and RMSE is larger than 0.02. The MODIS BBE derived from the Version 4.1 emissivity product was lower than the estimated BBE, and the bias and RMSE were less than 0.003 and 0.015, respectively. The estimated BBE was in good agreement with ASTER BBE, with a bias and RMSE of less than 0.001 and 0.012, respectively. Thus, the accuracy of the estimated BBE was higher than that derived from the MODIS emissivity products. Then the new algorithm was validated by field measurements. The validation results obtained from the three field measurements conducted in China indicated that the average difference between the estimated BBE and the measured BBE was 0.015. The validation results based on the measurements of five dune sites in western/southwestern U.S. indicated that the average difference between the estimated BBE and the measured BBE was 0.018. Overall, the average difference was 0.016.

Finally, we introduced a strategy for estimating global land surface BBEs and provided an example of a global BBE map. We have estimated the global 8 day 1 km land surface BBE from 2000 through 2010 using this strategy. This product was freely released to the public in November 2012 and can be ordered from the BNU Center for Global Change Data Processing and Analysis (http://www.bnu-datacenter.com) and Global Land Cover Facility (http://glcf.umd.edu).

Acknowledgments

The MODIS and ASTER data were obtained from https://wist.echo.nasa.gov/api/, and the soil taxonomy was obtained from http://soils.usda.gov/use/worldsoils/mapindex/order.html. Part of the validation data were downloaded from http://emissivity.jpl.nasa.gov/validation. The SimLab was downloaded from http://ipsc.jrc.ec.europa.eu/?id=756. This work was partly supported by the National Natural Science Foundation of China via Grants 41371323, 40901167, and 41331173, the National High Technology Research and Development Program of China via Grant 2013AA122801, and the Beijing Higher Education Young Elite Teacher project via Grant YETP0233.

References

Baldridge, A. M., S. J. Hook, C. I. Grove, and G. Rivera (2009), The ASTER spectral library version 2.0, *Remote Sens. Environ.*, *113*(4), 711–715.

Bonan, G. B., K. W. Oleson, M. Vertenstein, S. Levis, X. Zeng, Y. Dai, R. E. Dickinson, and Z. Yang (2002), The land surface climatology of the community land model coupled to the NCAR community climate model, *J. Clim.*, *15*, 3123–3149.

Borel, C. C. (2008), Error analysis for a temperature and emissivity retrieval algorithm for hyperspectral imaging data, *Int. J. Remote Sens.*, *29*(17–18), 5029–5045.

Cescatti, A., et al. (2012), Intercomparison of MODIS albedo retrievals and in situ measurements across the global FLUXNET network, *Remote Sens. Environ.*, *121*(0), 323–334, doi:10.1016/j.rse.2012.02.019.

Cheng, J., and S. Liang (2013), Estimating global land surface broadband thermal-infrared emissivity from the Advanced Very High Resolution Radiometer optical data, *Int. J. Digital Earth*, doi:10.1080/17538947.2013.783129.

Cheng, J., Q. Liu, X. Li, X. Qing, Q. Liu, and Y. Du (2008), Correlation-based temperature and emissivity separation algorithm, *Sci. China, Ser. D Earth Sci.*, *51*(3), 363–372.

Cheng, J., S. Liang, J. Wang, and X. Li (2010a), A stepwise refining algorithm of temperature and emissivity separation for hyperspectral thermal infrared data, *IEEE Trans. Geosci. Remote Sens.*, *48*(3), 1588–1597.

Cheng, J., S. Liang, F. Weng, J. Wang, and X. Li (2010b), Comparison of radiative transfer models for simulating snow surface thermal infrared emissivity, *IEEE J. Sel. Topics Appl. Earth Observ.*, *3*(3), 323–336.

Cheng, J., S. Liang, Y. Yao, and X. Zhang (2013), Estimating the optimal broadband emissivity spectral range for calculating surface longwave net radiation, *IEEE Geosci. Remote Sens. Lett.*, *10*(2), 401–405.

Cheng, J., S. Liang, Y. Yao, B. Ren, L. Shi, and H. Liu (2014), A comparative study of three land surface broadband emissivity datasets from satellite data, *Remote Sens.*, *6*, 111–134.

Dong, L. X., J. Y. Hu, S. H. Tang, and M. Min (2013), Field validation of GLASS Land Surface Broadband Emissivity Database using pseudo-invariant sand dunes sites in Northern China, *Int. J. Digital Earth*, doi:10.1080/17538947.17532013.17822573.

Gillespie, A. R. (1985), Lithologic mapping of silicate rocks using TIMS, in *Proc. TIMS Data Users' Workshop*, edited, pp. 29–44.

Gillespie, A. R., S. Rokugawa, T. Matsunaga, J. S. Cothern, S. J. Hook, and A. B. Kahle (1998), A temperature and emissivity separation algorithm for Advanced Spaceborne Thermal Emission and Reflection Radiometer (ASTER) images, *IEEE Trans. Geosci. Remote Sens.*, *36*, 1113–1126.

Gillespie, A. R., E. A. Abbott, L. Gilson, G. Hulley, J.-C. Jimenez-Munoz, and J. A. Sobrino (2011), Residual errors in ASTER temperature and emissivity products AST08 and AST05, *Remote Sens. Environ.*, *115*, 3681–3694.

Griend, A. A. V. D., and M. Owe (1993), On the relationship between thermal emissivity and the normalized difference vegetation index for natural surfaces, *Int. J. Remote Sens.*, *14*(6), 1119–1131.

Hori, M., et al. (2006), In-situ measured spectral directional emissivity of snow and ice in the 8–14 um atmospheric window, *Remote Sens. Environ.*, *100*, 486–502.

Hulley, G. C., and S. J. Hook (2009), Intercomparison of versions 4, 4.1 and 5 of the MODIS land surface temperature and emissivity products and validation with laboratory measurements of sand samples from the Namib desert, Namibia, *Remote Sens. Environ.*, *113*, 1313–1318.

Hulley, G. C., S. J. Hook, and A. M. Baldridge (2009), Validation of the North American ASTER Land Surface Emissivity Database (NAALSED) version 2.0 using pseudo-invariant sand dune sites, *Remote Sens. Environ.*, *113*, 2224–2233.

Hulley, G. C., S. J. Hook, and A. M. Baldridge (2010), Investigating the effects of soil moisture on thermal infrared land surface temperature and emissivity using satellite retrievals and laboratory measurements, *Remote Sens. Environ.*, *114*, 1480–1493.

Jacob, F., F. Petitcolin, T. Schmugge, E. Vermote, A. French, and K. Ogawa (2004), Comparison of land surface emissivity and radiometric temperature derived from MODIS and ASTER sensors, *Remote Sens. Environ.*, *90*(2), 137–152.

Jin, M., and S. Liang (2006), An improved land surface emissivity parameter for land surface models using global remote sensing observations, *J. Clim.*, *19*, 2867–2881.
Kanani, K., L. Poutier, F. Nerry, and M.-P. Stoll (2007), Directional effects consideration to improve out-doors emissivity retrieval in the 3–13 um domain, *Optic. Express*, *15*(19), 12,464–12,482.
Li, Z.-L., and F. Becker (1993), Feasibility of land surface temperature and emissivity determination from AVHRR data, *Remote Sens. Environ.*, *43*, 67–85.
Li, Z.-L., H. Wu, N. Wang, S. Qiu, J. A. Sobrino, Z.-M. Wan, B.-H. Tang, and G.-J. Yan (2013), Land surface emissivity retrieval from satellite data, *Int. J. Remote Sens.*, *34*(9–10), 3084–3127.
Liang, S. (2001), An optimization algorithm for separating land surface temperature and emissivity from multispectral thermal infrared imagery, *IEEE Trans. Geosci. Remote Sens.*, *39*, 264–274.
Liang, S. (2004), *Quantitative Remote Sensing of Land Surface*, 534 pp., John Wiley and Sons, Inc., Jew Jersey.
Liang, S. (2011), Review on estimation of land surface radiation and energy budgets from ground measurement, remote sensing and model simulations, *IEEE J. Sel. Topics Appl. Earth Observ.*, *3*, 225–240.
Liang, S., H. Fang, M. Chen, C. J. Shuey, C. Walthall, C. Daughtry, J. Morisette, C. Schaaf, and A. Strahler (2002), Validating MODIS land surface reflectance and albedo products: Methods and preliminary results, *Remote Sens. Environ.*, *83*(1–2), 149–162.
Liang, S., W. Kustas, G. Schaepman-Strub, and X. Li (2010), Impacts of climate change and land use change on land surface radiation and energy budgets, *IEEE J. Sel. Topics Appl. Earth Observ.*, *3*(3), 219–224.
Liang, S., et al. (2013), A long-time Global LAnd Surface Satellite (GLASS) data-set for environmental studies, *Int. J. Digital Earth*, *6*(S1), 5–33.
Mira, M., E. Valor, R. Boluda, V. Caselles, and C. Coll (2007), Influence of soil water content on the thermal infrared emissivity of bare soils: Implication for land surface temperature determination, *J. Geophys. Res.*, *112*, F04003, doi:10.1029/2007JF000749.
Momeni, M., and M. R. Saradjian (2007), Evaluating NDVI-based emissivities of MODIS bands 31 and 32 using emissivities derived by day/night LST algorithm, *Remote Sens. Environ.*, *106*(2), 190–198.
Mushkin, A., and A. R. Gillespie (2005), Estimating sub-pixel surface roughness using remotely sensed stereoscopic data, *Remote Sens. Environ.*, *99*(1–2), 75–83.
Nerry, F., J. Labed, and M.-P. Stoll (1988), Emissivities signatures in the thermal IR band for remote sensing: Calibration procedure and method of measurements, *Appl. Opt.*, *27*(4), 758–764.
Ogawa, K., and T. Schmugge (2004), Mapping surface broadband emissivity of the Sahara desert using ASTER and MODIS data, *Earth Interact.*, *8*, 1–14.
Ogawa, K., T. Schmugge, F. Jacob, and A. French (2003), Estimation of land surface window (8–12 um) emissivity from multi-spectral thermal infrared remote sensing—A case study in a part of Sahara Desert, *Geophys. Res. Lett.*, *30*(2), 1067, doi:10.1029/2002GL016354.
Ogawa, K., T. Schmugge, and S. Rokugawa (2008), Estimating broadband emissivity of arid regions and its seasonal variations using thermal infrared remote sensing, *IEEE Trans. Geosci. Remote Sens.*, *46*(2), 334–343.
Pequignot, E., A. Chedin, and N. A. Scott (2008), Infrared continental surface emissivity spectra retrieved from AIRS Hyperspectral sensor, *J. Appl. Meteoric. Climatol.*, *47*, 1619–1633.
Peres, L. F., and C. C. DaCamara (2005), Emissivity maps to retrieve land-surface temperature from MSG/SEVIRI, *IEEE Trans. Geosci. Remote Sens.*, *43*(8), 1834–1844, doi:10.1109/tgrs.2005.851172.
Peres, L. F., and C. C. DaCamara (2006), Improving two-temperature method retrievals based on a nonlinear optimization approach, *IEEE Geosci. Remote Sens. Lett.*, *3*(2), 232–236.
Ren, H., S. Liang, G. Yan, and J. Cheng (2013), Empirical algorithms to map global broadband emissivities over vegetated surfaces, *IEEE Trans. Geosci. Remote Sens.*, *51*(5), 2619–2631, doi:10.1109/TGRS.2012.2216887.
Román, M. O., et al. (2009), The MODIS (Collection V005) BRDF/albedo product: Assessment of spatial representativeness over forested landscapes, *Remote Sens. Environ.*, *113*(11), 2476–2498, doi:10.1016/j.rse.2009.07.009.
Saltelli, A., S. Tarantola, and K. P.-S. Chan (1999), A quantitative model-independent method for global sensitivity analysis of model output, *Technometrics*, *41*(1), 39–56.
Schaaf, C. B., et al. (2002), First operational BRDF, albedo nadir reflectance products from MODIS, *Remote Sens. Environ.*, *83*, 135–148.
Sellers, P. J., et al. (1997), Modeling the exchange of energy, water and carbon between the continents and the atmosphere, *Science*, *275*, 502–509.
Sobrino, J. A., J. C. Jimenez-Munoz, P. J. Zarco-Tejada, G. Sepulcre-Canto, and E. D. Miguel (2006), Land surface temperature derived from airborne hyperspectral scanner thermal infrared data, *Remote Sens. Environ.*, *102*(1–2), 99–115.
Sobrino, J. A., J. C. Jiménez-Muñoz, G. Sòria, M. Romaguera, L. Guanter, J. Moreno, A. Plaza, and P. Martinez (2008), Land surface emissivity retrieval from different VNIR and TIR sensors, *IEEE Trans. Geosci. Remote Sens.*, *46*, 316–327.
Tang, B.-H., H. Wu, C. Li, and Z.-H. Li (2011), Estimation of broadband surface emissivity from narrowband emissivities, *Optic. Express*, *19*(1), 185–192.
Tsvetsinskaya, E. A., C. B. Schaaf, F. Gao, A. H. Strahler, R. E. Dickinson, X. Zeng, and W. Lucht (2002), Relating MODIS-derived surface albedo to soils and rock types over Northern Africa and Arabian peninsula, *Geophys. Res. Lett.*, *29*(9), 1353, doi:10.1029/2001GL014096.
Valor, E., and V. Caselles (1996), Mapping land surface emissivity from NDVI: Application to European, African, and South American areas, *Remote Sens. Environ.*, *57*(3), 167–184.
Wan, Z., and Z.-L. Li (1997), A physics-based algorithm for retrieving land-surface emissivity and temperature from EOS/MODIS data, *IEEE Trans. Geosci. Remote Sens.*, *35*(4), 980–996.
Wang, K., and S. Liang (2009), Evaluation of ASTER and MODIS land surface temperature and emissivity products using long-term surface longwave radiation observations at SURFRAD sites, *Remote Sens. Environ.*, *113*(7), 1556–1565.
Wang, K., J. Liu, X. Zhou, M. Sparrow, M. Ma, Z. Sun, and W. Jiang (2004), Validation of the MODIS global land surface albedo product using ground measurements in a semidesert region on the Tibetan Plateau, *J. Geophys. Res.*, *109*, D05107, doi:10.1029/2003JD004229.
Wang, K., Z. Wan, P. Wang, M. Sparrow, J. Liu, X. Zhou, and S. Haginoya (2005), Estimation of surface long wave radiation and broadband emissivity using Moderate Resolution Imaging Spectroradiometer (MODIS) land surface temperature/emissivity products, *J. Geophys. Res.*, *110*, D11109, doi:10.1029/2004JD005566.
Wang, Z., C. B. Schaaf, M. J. Chopping, A. H. Strahler, J. Wang, M. O. Román, A. V. Rocha, C. E. Woodcock, and Y. Shuai (2012), Evaluation of Moderate-resolution Imaging Spectroradiometer (MODIS) snow albedo product (MCD43A) over tundra, *Remote Sens. Environ.*, *117*, 264–280, doi:10.1016/j.rse.2011.10.002.
Wilber, A. C., D. P. Kratz, and S. K. Gupta (1999), Surface emissivity maps for use in satellite retrievals of longwave radiation, *NASA Tech. Publ.*, *NASA/TP-1999-209362* [Available online at http://techreports.larc.nasa.gov/1trs].
Xiao, Q., Q. H. Liu, X. W. Li, L. F. Chen, Q. Liu, and X. Z. Xin (2003), A field measurements method of spectral emissivity and research on the feature of soil thermal infrared emissivity, *Int. J. Infrared Millimet Waves*, *22*(5), 373–378.

Zhang, Y., Y. Li, Z. Rong, X. Hu, L. Zhang, and J. Liu (2009), Field measurement of Gobi surface emissivity spectrum at Dunhuang calibration site of China, *Spectrosc. Spect. Anal.*, *29*(5), 1213–1217.

Zhou, L., R. E. Dickinson, K. Ogawa, Y. Tian, M. Jin, and T. Schmugge (2003a), Relations between albedos and emissivities from MODIS and ASTER data over North African Desert, *Geophys. Res. Lett.*, *30*(20), 2026, doi:10.1029/2003GL018069.

Zhou, L., R. E. Dickinson, Y. Tian, M. Jin, K. Ogawa, H. Yu, and T. Schmugge (2003b), A sensitivity study of climate and energy balance simulations with use of satellite-based emissivity data over northern Africa and the Arabian peninsula, *J. Geophys. Res.*, *108*(D24), 4795, doi:10.1029/2003JD004083.